Acta Pharmaceutica Sinica B 2024;14(5):2317–2332

Chinese Pharmaceutical Association
Institute of Materia Medica, Chinese Academy of Medical Sciences

Acta Pharmaceutica Sinica B

www.elsevier.com/locate/apsb
www.sciencedirect.com

ORIGINAL ARTICLE

In situ autophagy regulation in synergy with phototherapy for breast cancer treatment

Huijuan Zhang[a,b,c], Xiangyang Xuan[a], Yaping Wang[a], Zijun Qi[a], Kexuan Cao[a], Yingmei Tian[a], Chaoqun Wang[a], Junbiao Chang[c,d,*], Zhenzhong Zhang[a,b,*], Lin Hou[a,b,*]

[a]*School of Pharmaceutical Sciences, Zhengzhou University, Zhengzhou 450001, China*
[b]*Key Laboratory of Targeting Therapy and Diagnosis for Critical Diseases, Zhengzhou 450001, China*
[c]*Collaborative Innovation Center of New Drug Research and Safety Evaluation, Zhengzhou 450001, China*
[d]*School of Chemistry and Molecular Engineering, Zhengzhou University, Zhengzhou 450001, China*

Received 13 August 2023; received in revised form 24 October 2023; accepted 25 October 2023

KEY WORDS

Autophagy;
Tumor phototherapy;
Synergistic sensitization;
HCQ;
TRANSFERRIN;
Disulfide bond reconstruction;
GSH;
Biomimetic mineralized nano-tellurium

Abstract Autophagy is an important factor in reducing the efficacy of tumor phototherapy (including PTT and PDT). Accurate regulation of autophagy in tumor cells is a new strategy to improve the anti-tumor efficiency of PTT/PDT. This project intended to construct a tumor-activated autophagy regulator to efficiently block PTT/PDT-induced autophagy and realize synergistic sensitization to tumor phototherapy. To achieve this goal, we first synthesized TRANSFERRIN (Tf) biomimetic mineralized nano-tellurium (Tf-Te) as photosensitizer and then used disulfide bond reconstruction technology to induce Tf-Te self-assembly. The autophagy inhibitor hydroxychloroquine (HCQ) and iron ions carried by Tf were simultaneously loaded to prepare a tumor-responsive drug reservoir Tf-Te/HCQ. After entering breast cancer cells through the "self-guidance system", Tf-Te/HCQ can generate hyperpyrexia and ROS under NIR laser irradiation, to efficiently induce PTT/PDT effect. Meanwhile, the disulfide bond broke down in response to GSH, and the nanoparticles disintegrated to release Fe^{2+} and HCQ at fixed points. They simultaneously induce lysosomal alkalinization and increased osmotic pressure, effectively inhibit autophagy, and synergistically enhance the therapeutic effect of phototherapy. *In vivo* anti-tumor results have proved that the tumor inhibition rate of Tf-Te/HCQ can be as high as 88.6% on 4T1 tumor-bearing mice. This multifunctional drug delivery system might provide a new alternative for more precise and effective tumor phototherapy.

*Corresponding authors.
E-mail addresses: jbchang@public.zz.ha.cn (Junbiao Chang), zzzhang_zzu@163.com (Zhenzhong Zhang), houlin_pharm@163.com (Lin Hou).
Peer review under the responsibility of Chinese Pharmaceutical Association and Institute of Materia Medica, Chinese Academy of Medical Sciences.

https://doi.org/10.1016/j.apsb.2023.11.019

1. Introduction

Compared with the traditional cancer treatment methods, the photothermal/photodynamic (PTT/PDT) synergistic therapy strategy has aroused extensive interest because it is a non-invasive local treatment method with fewer side effects[1]. Although some photosensitizers and photothermal agents have exhibited good anti-tumor effects, there are still many common shortcomings that limit their further *in vivo* application, such as poor stability, low photon efficiency, and potential biotoxicity. As an inorganic nanomaterial, Tellurium (Te) has shown great potential in the biomedical application field[2−4]. Recently, studies have shown that Te nanoparticles (NPs) synthesized by biomimetic mineralization strategy have unique advantages, such as excellent biocompatibility, good photostability, high photothermal conversion, and reactive oxygen species (ROS) production efficiency[5,6]. Meanwhile, biomimetic mineralized Te NPs using natural PROTEINS (such as human serum ALBUMIN) with small particle size can be rapidly cleared by the kidney after playing a role, which effectively solves the problem of biological toxicity caused by the accumulation of inorganic photosensitizer in the body[7].

The hyperpyrexia and ROS produced by Te NPs under laser irradiation can cause oxidative stress to damage tumor cells[8], and then generate a large amount of fragmented DNA, toxic PROTEINS, and damaged organelles. To defend against this unfavorable condition, tumor cells activate autophagy to initiate a self-repair program, and then reduce the PTT/PDT synergistic therapy effect[9−13]. In addition, studies have proved that autophagosomes encapsulating abnormal substances must be fused with lysosomes to form autophagolysosomes, so as to realize the recovery and utilization of damaged cell components, which is known as a lysosome-dependent cellular metabolic pathway[14]. As a classic autophagy inhibitor, HCQ can induce deacidification of lysosomes and destroy the detoxification function of autophagolysosomes, which will cut off the self-protection pathway of tumor cells under severe oxidative stress state and sensitize the PTT/PDT anti-tumor effect[15]. However, HCQ has no tissue-targeting ability and cell selectivity. To precisely regulate the autophagy of tumor cells, tumor-targeting drug carriers should be designed reasonably.

Studies have proved that the expression of the TRANSFERRIN receptor (TfR) on the surface of tumor cells is much higher than that of normal cells. As the specific ligand of TfR, Tf has natural tumor-targeted recognition property[16−19]. Besides, Tf is also an excellent drug carrier with a specific channel on its surface, which is universal for small molecule drug loading[20]. Based on the above characteristics, natural Tf can be simultaneously used as the biomimetic mineralization template for Te and a drug carrier for HCQ, to realize their targeted delivery to tumor.

Once the nanosystem reaches tumor cells, how to release drugs quickly to exert therapeutic effect is another key issue, which requires the construction of a more intelligent tumor "on-off" drug reservoir[21,22]. The concentration of reduced GSH in tumor cells (5−10 mmol/L) was significantly higher than that of in blood (0 μmol/L) and extracellular tumor environment (2−20 μmol/L)[23,24]. Therefore, GSH can be used as the "trigger" to design a tumor "on-off" drug delivery system. ALBUMIN molecules contain 17 disulfide bonds. Saleh et al.[25] used disulfide bond reconstruction technology to prepare curcumin-loaded ALBUMIN nanoparticles, which exhibited good stability and GSH-responsive drug release profile. Luo et al.[26] prepared a DOX and Ce6 co-loaded hybrid protein (albumin and hemoglobin) oxygen carrier, which can release drugs in response to GSH to achieve combined tumor PDT-chemotherapy. Furthermore, the above two studies showed that reconstituted nanoparticles still maintain the corresponding physiological functions and active recognition ability of albumin on the gp60 receptor expressed by tumor cells. There are 19 disulfide bonds in the Tf molecule, which means that Tf may become an excellent drug carrier with GSH responsiveness by using disulfide bond reconstruction technology[27,28].

Based on the above background, we designed a tumor-activated autophagy regulator to efficiently block PTT/PDT-induced autophagy for the synergistic therapy of breast cancer. In this study, natural Tf was simultaneously used as the biomimetic mineralization template for Te and the drug carrier for HCQ. As Scheme 1A shown, while inducing the self-assembly of Tf-Te, autophagy inhibitor HCQ was loaded synchronously to construct tumor-activated nano drug delivery system Tf-Te/HCQ, through the disulfide bond reconstruction technology (to convert intramolecular disulfide bonds into intermolecular disulfide bonds). After entering tumor cells *via* Tf "navigation", Tf-Te/HCQ will generate hyperpyrexia and ROS under NIR laser irradiation, realizing PDT/PTT combined treatment of breast cancer. At the same time, the high level of GSH in tumor cells breaks intermolecular disulfide bonds of Tf-Te/HCQ to release HCQ and Fe^{2+} at the fixed point. Subsequently, HCQ and Fe^{2+} act synchronously on lysosomes to increase their pH and osmotic pressure, thereby inhibiting lysosomal autophagy and synergistically enhancing the therapeutic effect of tumor phototherapy (Scheme 1B).

2. Materials and methods

2.1. Materials

Sodium tellurite (Na_2TeO_3, 99.9%), reduced GSH (98%) and Tf were purchased from Shanghai Aladdin Biochemical Technology Co., Ltd. (Shanghai, China). Hydroxychloroquine sulfate ($HCQ·H_2SO_4$, 99%) was acquired from Adamas-Beta Reagents Co., Ltd. (Shanghai, China). Sodium hydroxide (NaOH, 95%), Sodium chloride (NaCl, 99.5%), and Ethylacetate (99%) were gained from Shanghai Yi En Chemical Technology Co., Ltd.

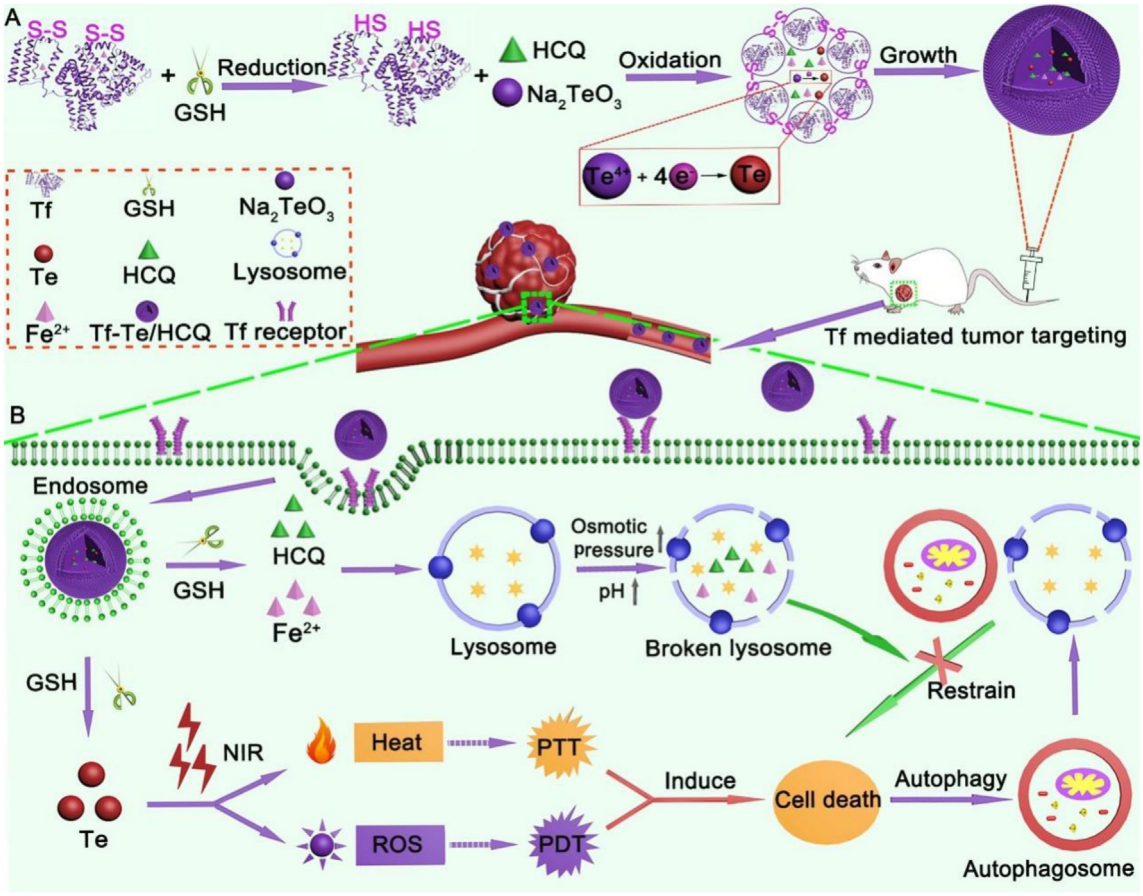

Scheme 1 (A) The synthesis principle of Tf-Te/HCQ. (B) The synergistic anti-tumor mechanism of Tf-Te/HCQ.

(Shanghai, China). The sulfhydryl assay kit was bought from Solarbio Science & Technology Co., Ltd. (Beijing, China). Fluorescein isothiocyanate (FITC, ≥95%) was obtained from Shanghai Aladdin Biochemical Technology Co., Ltd. (Shanghai, China). Rabbit anti-LC3B and rabbit anti-SQSTM1/p62 antibodies were obtained from Beijing Boosen Biotechnology Co., Ltd. (Beijing, China). The reactive oxygen species detection kit and Cell Counting Kit-8 were obtained from Biyuntian Biotechnology Co., Ltd. (Shanghai, China). Rabbit IgG/Cy3 was obtained from Wuhan Xavier Biotechnology Co., Ltd. (Wuhan, China). Calcein-AM/PI double stain kit was bought from Yi Sheng Biotechnology Shanghai Co., Ltd. (Shanghai, China).

2.2. *Synthesis of Tf-Te NPs*

Firstly, dissolve 7 mg of GSH and 16 mg of Tf in 1 mL of deionized water to prepare GSH and Tf aqueous solutions, respectively. Next, add Tf solution to the GSH aqueous solution slowly drop by drop. Thereafter, 5 mg of Na_2TeO_3 was dissolved in 0.4 mL of deionized water and then added into the above solution slowly. After stirring for 12 h at room temperature, the product was transferred to a dialysis bag (MW = 100 kD) and dialyzed with water for 24 h to obtain purified Tf-Te NPs.

2.3. *Synthesis of Tf-Te/HCQ*

Firstly, hydrophobic HCQ was loaded into the hydrophobic cavity of Tf. In brief, dissolve 7 mg of GSH and 16 mg of Tf in 1 mL of deionized water to prepare GSH and Tf aqueous solutions, respectively. Next, add Tf solution into the GSH aqueous solution slowly drop by drop. After stirring at 37 °C for 60 min, the intramolecular S−S disulfide bonds opened to obtain a homogeneous solution of Tf with spatial structure unfolding. Subsequently, 4 mg of HCQ was dissolved in 0.4 mL of anhydrous ethanol and then dropped into the above Tf solution slowly. After stirring for 12 h, HCQ was efficiently loaded into the hydrophobic cavity of Tf. Secondly, 5 mg of Na_2TeO_3 was dissolved in 0.4 mL of deionized water, and then slowly added to the above solution. After further stirring for 12 h at room temperature, the mixture solution was placed into a dialysis bag (MW = 100 kD) and dialyzed with deionized water for 24 h to obtain Tf-Te/HCQ.

2.4. *Characterization of Tf-Te and Tf-Te/HCQ*

The morphological feature of NPs was monitored by transmission electron microscopy (TEM, JEM 1200EX, Jeol, Japan). The particle size distribution and zeta potential of NPs were measured by dynamic light scattering (DLS, Zetasizer Nano ZS-90, Malvern, UK). The spectroscopic characteristics of NPs were analyzed using the ultraviolet−visible spectrophotometer (UV−Vis, UV-2550, Shimadzu, Japan). The chemical composition and crystal structure of Te were investigated by X-ray photoelectron spectroscopy (XPS, Thermo escalab 250XI, Thermofisher, USA) and X-ray diffract meter (XRD, BRUCKER D8, Brucker, Germany), respectively.

2.5. Determination of drug loading and encapsulation efficiency

For the load of HCQ, 0.4 mL of free HCQ (10 mg/mL) absolute ethanol solution and 2 mL of Tf (8 mg/mL) aqueous solution treated with 1 mL of GSH (8 mg/mL) were mixed and stirred for 12 h. Thereafter, Na_2TeO_3 (12.5 mg/mL) was added to the above mixture for stirring fully. Subsequently, the Tf-Te/HCQ nanosuspension was dialyzed with water (MW = 3.5 kD) for 24 h to remove unloaded free HCQ. The loading and encapsulation efficiency of HCQ in Tf-Te/HCQ was determined as follows. GSH (2 mg/mL) was added to Tf-Te/HCQ suspension and stirred for 12 h to destroy the nanosystem for HCQ release, and then HCQ containing supernatant was collected by high-speed centrifugation (10,000 rpm, 5 min, TGL-16G table-top centrifuge, Shanghai, China). After that, the concentration of loaded HCQ was measured at 343 nmol/L by UV−Vis spectrophotometer (Shimadzu, Kyoto, Japan). Finally, the encapsulation and loading efficiency was calculated as shown in Eqs. (1) and (2), respectively:

$$\text{Entrapment efficiency}(\%) = W_{\text{Loaded HCQ}} \big/ W_{\text{Totally added HCQ}} \times 100 \quad (1)$$

$$\text{Loading efficiency}\ (\%) = W_{\text{Loaded HCQ}} \,/\, W_{\text{Tf-Te/HCQNPs}} \times 100 \quad (2)$$

2.6. Drug release evaluation

The release behavior of HCQ from Tf-Te/HCQ was evaluated by the dialysis method. In brief, Tf-Te/HCQ nanosuspensions were sealed in dialysis bags (MW = 3.5 kD). Then, they were immersed in 45 mL of PBS buffer solution containing different concentrations of GSH (①0 mmol/L GSH; ② 20 μmol/L GSH; ③5 mmol/L GSH), and gently shaken in a constant temperature incubator (37 °C, 100 rpm). At pre-set time points, 2 mL of release medium was extracted and replaced with the same volume of corresponding fresh medium. The concentration of HCQ was measured at 343 nmol/L using a UV−Vis spectrophotometer to calculate the cumulative drug release percentage. Moreover, to visualize the disintegration of Tf-Te/HCQ in response to GSH, Tf-Te/HCQ nanoparticle immersed in a release medium containing 5 mmol/L GSH was observed using TEM (Jeol, Tokyo, Japan) at the end of the drug release experiment.

2.7. Measurement of photothermal and photodynamic performance

The photothermal performance of Tf-Te/HCQ was evaluated by the NIR laser at 808 nmol/L (Huxley Laser Technology Co., Ltd., Xian, China). Firstly, the effect of Tf-Te/HCQ concentration on photothermal performance was studied. In brief, 1.0 mL of Tf-Te/HCQ suspensions of various concentrations (0, 10, 30, 60, 90 μg/mL) were irradiated for 5 min (2 W/cm^2), and the temperature was recorded every 1 min using infrared thermal imaging thermometer (Ti-32, Fluke, USA). Secondly, the effect of laser power on photothermal performance was studied. Briefly, 1.0 mL of Tf-Te/HCQ suspension (30 μg/mL) was irradiated by NIR laser with different power (1, 1.5, 2, 2.5 W/cm^2) for 5 min, and the temperature was recorded every 1 min using infrared thermal imaging thermometer (Fluke, USA).

Subsequently, the photothermal stability properties of Tf-Te and Tf-Te/HCQ were investigated. 1.0 mL of Tf-Te/HCQ suspension (30 μg/mL) was irradiated by the NIR laser (2 W/cm^2) for 5 min. Meanwhile, deionized water with the same treatment was used as the control. The temperature was recorded every 1 min using an infrared thermal imaging thermometer. Once the NIR laser was turned off, Tf-Te/HCQ suspension cooled naturally to the ambient temperature, and the temperature of the Tf-Te/HCQ suspension was measured every 1 min during this cooling process. Repeat the above procedure five times. To calculate the photothermal conversion efficiency (η) of Tf-Te/HCQ, NIR laser (2 W/cm^2) was used to irradiate Tf-Te/HCQ suspension (30 μg/mL, 1.0 mL) and deionized water (1.0 mL) for 10 min, respectively. The suspensions cooled to ambient temperature naturally after turning off the laser. During the above cooling process, the temperature of Tf-Te/HCQ suspension and water was measured every 1 min. Finally, the photothermal conversion efficiency (η) of Tf-Te/HCQ was calculated as shown in Eqs. (3) and (4):

$$t = \frac{\sum_i m_i C_{P,i}}{hA} Ln(\theta) \quad (3)$$

$$\eta = \frac{hA\left(\Delta T_{\max,\text{mix}} \Delta T_{\max,\text{H}_2\text{O}}\right)}{I\left(1-10^{A_\lambda}\right)} \quad (4)$$

Next, the photodynamic performance of Tf-Te and Tf-Te/HCQ under NIR laser irradiation was investigated using a ROS detection kit. In brief, Tf-Te or Tf-Te/HCQ suspensions with different concentrations (1, 5, and 10 μg/mL) were prepared, and deionized water was used as the control group. 200 μL of each above solution was placed in the well of a 96-well plate and then mixed with 50 μL of ROS probe (10 μmol/L). After standing for 10 min at 37 °C in the dark, the laser group was irradiated with 808 nmol/L laser (2 W/cm^2) for 3 min (Fluke), and the fluorescence intensity was detected immediately under the enzyme-labeled instrument (Spectra Mr, DYNEX, USA), with the excitation wavelength of 488 nmol/L and the emission wavelength of 525 nmol/L. Moreover, electron spin resonance spectroscopy (ESR) was utilized to determine the specific type of ROS generated by Tf-Te/HCQ NPs under 808 nmol/L irradiation using 2,2,6,6-tetramethylpiperide (TEMP), 5-*tert*-butoxycarbonyl-5-methyl-1-pyrroline *N*-oxide (BMPO) and 5,5-dimethyl-1-pyrroline-*N*-oxide (DMPO) as the spin-trapping agents of singlet oxygen ($^1O_2$), superoxide radicals ($\bullet O_2$) and hydroxyl radicals (•OH), respectively. In brief, spectra of spin-trapped $^1O_2$, $\bullet O_2$ and •OH were acquired by mixing 5 μL of TEMP, BMPO, and DMPO (500 mmol/L) with 100 μL Tf-Te/HCQ suspension (Te = 10 μg/mL), respectively. Then the above mixture solution samples were irradiated under 808 nmol/L laser at 2.0 W/cm^2 for 3 min, followed by ESR analysis.

2.8. Cellular uptake

The cellular uptake behavior of FITC-labeled Tf-Te/HCQ in 4T1 cells was quantitatively investigated by flow cytometry. Briefly, free FITC and FITC-labeled Tf-Te/HCQ were co-incubated with 4T1 cells for 1, 4, and 6 h, respectively. Next, cells were washed 3 times with PBS, subjected to digestion and centrifugation to collect cells, and then redispersed in 200 μL of PBS for FCM measurement. In addition, CLSM (Leica TCS SP8, Leica, Germany) was used to visually observe the cellular uptake behavior of Tf-Te/HCQ by RAW264.7 macrophages and 4T1 cells.

2.9. Cell inhibition rate assay

4T1 cells were seeded in 96-well plates (8×10^3 cells/well) and incubated overnight. Then cells were treated with different concentrations of HCQ, Tf-Te, and Tf-Te/HCQ for 6 h. Subsequently, cells were washed and continued to incubate with 200 μL of fresh culture medium for 24 h. In the above three groups, the concentrations of HCQ (0, 0.1, 0.5, 1, 5, 10 μg/mL) and Te (0, 0.1, 0.5, 1, 5, 10 μg/mL) were the same. For laser irradiation groups, cells were irradiated with 808 nmol/L laser (2 W/cm^2, 3 min) at 6 h after administration and then continued to culture for 24 h. Finally, the cell inhibition rate was determined by CCK8 method and calculated using the following Eq. (5):

$$\text{Cell inhibition rate}(\%) = \left(1 - \text{OD}_{\text{Experimental group}} / \text{OD}_{\text{Control group}}\right) \times 100 \quad (5)$$

Moreover, the HC11 cell (mouse mammary epithelial cell line) was chosen to explore the toxicity of Tf-Te/HCQ to normal cells. In brief, HC11 cells were seeded in 96-well plates (8×10^3 cells/well) and incubated overnight. After being treated with different concentrations of Tf-Te/HCQ for 6 h, cells were washed and continued to incubate with fresh culture medium for 24 h. For laser irradiation groups, cells were irradiated with 808 nmol/L laser (2 W/cm^2, 3 min) at 6 h after administration and then continued to culture for 24 h. Finally, the cell survival rate was determined by the CCK8 method.

2.10. Measurement of intracellular ROS

The DCFH-DA probe was used to measure intracellular ROS generation. Briefly, 4T1 cells were seeded in 6-well plates (3×10^5 cells/well) and incubated for 24 h. Next, cells were treated with fresh culture medium containing Tf-Te and Tf-Te/HCQ (Te = 10 μg/mL and HCQ = 10 μg/mL) for 6 h. After that, the old medium was replaced with a serum-free medium containing DCFH-DA (10 μmol/L). After incubation for 20 min, cells were irradiated for 3 min under NIR laser (2 W/cm^2). After another 20 min in the dark, cells were washed with PBS 3 times and fluorescent images were recorded using the fluorescence microscope (IX53, OLYMPUS, Japan). Finally, the semi-quantitative analysis of fluorescent intensity was carried out by ImageJ software (Rawak Software Inc., Germany).

2.11. Intracellular photothermal conversion ability of Tf-Te/HCQ

4T1 cells were seeded into 24-well plates at a density of 2×10^4 cells/well and incubated for 24 h. Next, cells were treated with fresh medium containing Tf-Te and Tf-Te/HCQ (10 μg/mL) for 6 h, respectively. After that, cells were irradiated with an 808 nmol/L laser (2 W/cm^2) for 3 min. Thermal images were recorded using infrared thermal imaging cameras before and after laser irradiation.

2.12. Study on co-delivery of intracellular HCQ and Fe^{2+}

By detecting the concentration changes of HCQ and Fe^{2+} in 4T1 tumor cells at different time points, the ability of Tf-Te/HCQ to synchronously co-deliver HCQ and Fe^{2+} was explored. 4T1 cells were seeded in cell culture dishes at a density of 8×10^5 cells/dish and incubated overnight. Then, cells were treated with Tf-Te/HCQ (HCQ: 10 μg/mL) for 1, 4, and 6 h, respectively. Thereafter, cells were collected and crushed at different time points to extract HCQ and Fe^{2+}. Finally, the intracellular concentrations of HCQ and Fe^{2+} were determined by HPLC (Waters e2695, Waters, USA) and Fe^{2+} detection kit, respectively.

2.13. Lysosome colocalization study

The localization performance of Tf-Te/HCQ in lysosomes was studied by CLSM. Firstly, 4T1 cells were seeded on a coverslip in 6-well plates (3×10^5 cells/well) and incubated overnight. Subsequently, the old medium was replaced with fresh medium containing FITC or FITC labeled Tf-Te/HCQ (FITC: 10 μg/mL) and incubated for 1, 4, and 6 h, respectively. Then cells were washed with PBS 3 times and stained with Lyso-Tracker Red (150 nmol/L) and Hoechst 33342 (5 μg/mL) for 40 and 15 min, to label the lysosome and nuclei, respectively. Finally, CLSM was used to record the colocalization performance of Tf-Te/HCQ with lysosomes.

2.14. Detection of intracellular pH

The autophagy inhibition effect induced by HCQ is achieved by alkalizing lysosomes, so the BCECF-AM pH fluorescence indicator was used to measure the change of intracellular pH. In brief, 4T1 cells (3×10^5 cells/well) were inoculated in 6-well plates for 24 h. The cells in the laser irradiation group were irradiated with 808 nmol/L laser (2 W/cm^2) for 3 min. After that, cells were treated with free HCQ, Tf-Te, and Tf-Te/HCQ (HCQ: 10 μg/mL) for 6 h, respectively. Next, cells were washed with PBS and then incubated with 1 mL of BCECF-AM (2 μmol/L) for 30 min. Finally, cells were washed with fresh culture medium and placed under a fluorescence microscope to record the results.

2.15. Study on lysosome damage

4T1 cells were inoculated into confocal small dishes at a density of 3×10^5 cells/well and incubated for 24 h. Thereafter, cells were treated with HCQ, Tf-Te, and Tf-Te/HCQ (HCQ: 10 μg/mL) for 6 h, respectively. For laser irradiation groups, cells were irradiated with 808 nmol/L laser (2 W/cm^2, 3 min) at 6 h after administration and then continued to culture for 24 h. After that, the old medium was replaced with a fresh medium. After being fixed with 4% paraformaldehyde, cells were stained with Lyso-Tracker Red (150 nmol/L) and Hoechst 33342 (5 μg/mL) for 40 and 15 min, to label the lysosome and nuclei, respectively. Finally, cells were washed with PBS and then placed under CLSM to record the results. To directly study the lysosomal damage effect induced by Fe^{2+}, 4T1 cells were incubated with different concentrations of Fe^{2+} for 6 h. After fixation, lysosomes and nuclei were labeled with Lyso-Tracker Red and Hoechst 33342, respectively. Finally, cells were washed and photographed using CLSM.

2.16. Measure the expression of autophagy-related proteins

Herein, the Western blot method was used to measure the expression of autophagy-related proteins through the following experimental steps. 4T1 cells were seeded in 6-well plates at a density of 3×10^5 cells/well and incubated overnight. Then, cells were treated with HCQ, Tf-Te, and Tf-Te/HCQ (HCQ: 10 μg/mL) for 6 h, respectively. For laser irradiation groups, cells were irradiated with 808 nmol/L laser (2 W/cm^2, 3 min) at 6 h after

administration and then continued to culture for 24 h. Thereafter, cells were washed with PBS three times. Next, the protein in 4T1 cells was collected after digestion and centrifugation. After that, the expression level of autophagy-related protein (p62 and LC3) was measured using a standard Western blot experiment operation procedure. Finally, the band strength was quantified using ImageJ software, and the protein expression was normalized to β-actin.

In addition, the immunofluorescence analysis method was also used to investigate the expression of p62 and LC3 in 4T1 cells. 4T1 cells were seeded on coverslips in 6 well plates (3×10^5 cells/well) and incubated overnight. Thereafter, cells were treated with HCQ, Tf-Te, and Tf-Te/HCQ for 6 h (HCQ: 10 μg/mL), respectively. Next, cells were washed with PBS and irradiated with NIR laser (2 W/cm^2) for 3 min. After that, cells were fixed with 4% paraformaldehyde for 20 min, washed with PBS 3 times, and treated with Triton X-100 immunostaining permeabilization buffer for 10 min. Subsequently, cells were washed and then incubated with QuickBlockTM Blocking Buffer for 15 min. After being treated with primary antibody and fluorescent dye-labeled secondary antibody, cells were further stained with Hoechst 33342 (5 μg/mL) for 15 min to label the nuclei. Finally, the fluorescent images were recorded under the CLSM.

2.17. *Tumor targeting ability and metabolism behavior of Tf-Te/HCQ in vivo*

Firstly, the biodistribution behavior of Tf-Te/HCQ was studied. Tf-Te/HCQ was labeled with IR780 (Tf-Te/HCQ@IR780) to monitor its real-time distribution *in vivo*. 4T1 tumor-bearing mice were injected with free IR780 and Tf-Te/HCQ@IR780 (IR780: 1 mg/kg) through the tail vein, respectively. At the pre-set time points (1, 2, 4, 8, 12, 24 h), fluorescence images of mice were recorded using an *in vivo* imaging system FX PRO (FX PRO, Kodak, USA). Next, to evaluate the tumor-targeting ability of Tf-Te/HCQ, the model mice were randomly divided into two groups: (1) IR780, and (2) Tf-Te/HCQ@IR780. The dosage of IR780 was 1 mg/kg. At 24 h post-injection, the mice were sacrificed. Then the main organs (heart, liver, spleen, lung, and kidney) and tumors were excised for *ex vivo* imaging using the FX PRO system. In addition, to investigate the dynamic distribution behavior of Tf-Te/HCQ in main tissues, heart, liver, spleen, lung, and kidney tissues of mice were collected at 1, 2, 4, and 12 h after intravenous administration of Tf-Te/HCQ@IR780 (IR780: 1 mg/kg) for *ex vivo* imaging. Finally, Image J software was used to calculate the fluorescence intensity. Furthermore, the metabolism behavior of Te in mice was explored using an ICP emission spectrometer. In brief, mice were administrated with Tf-Te/HCQ (Te: 1 mg/kg) through the tail vein. At the pre-set time points (0.5, 1, 2, 4, 8, 12, 24, 48 h), 20 μL of blood was collected through the eye socket for ICP analysis.

2.18. *In vivo antitumor effect*

When the tumor volume was close to 100 mmol/L^3, 4T1 tumor-bearing mice were randomly divided into 7 groups ($n = 6$): (1) control, (2) control + laser, (3) HCQ + laser, (4) Tf-Te, (5) Tf-Te + laser, (6) Tf-Te/HCQ, (7) Tf-Te/HCQ + laser. Various formulations were administered *via* the tail vein every 2 days for 7 times. In the above administration groups, the dosages of HCQ and Te were 2 and 1 mg/kg, respectively. For the control group, tumor-bearing mice were administrated with saline. For laser irradiation groups, tumor tissues were irradiated with 808 nmol/L laser (2 W/cm^2, 1 min) at 8 h after administration. The body weights and tumor volumes were monitored before injection every time. The tumor volume was calculated according to the following formula $(A \times B^2)/2$, where A represented the larger diameter and B represented the smaller one. The relative tumor volume was calculated as V/V_0, where V and V_0 represented the tumor volume during the treatment period and at the beginning of treatment, respectively. At the end of treatment, the mice were sacrificed. And then tumors and major organs (heart, liver, spleen, lung, and kidney) were collected for H&E and immunofluorescence staining, to evaluate the histopathological changes and tumor autophagy inhibition effect.

2.19. *ROS level and photothermal conversion effect in tumor tissue*

ROS level in tumor tissues was detected using ROS fluorescent probe DCFH-DA. In brief, saline (Control group), HCQ, Tf-Te, and Tf-Te/HCQ were injected through the tail vein. In the above administration groups, the dosages of HCQ and Te were 2 and 1 mg/kg, respectively. 8 h after administration, NIR laser (2 W/cm^2) was adopted to irradiate the tumor tissue for 1 min. After laser irradiation, the tumor tissues were collected and stored at −80 °C to prepare frozen slices. After double staining with DCFH-DA and DAPI, the slices were placed under a fluorescence microscope (OLYMPUS, Tokyo, Japan) to record the ROS level in the tumor.

Next, the photothermal conversion effect of Tf-Te/HCQ in tumor tissue was further explored. Briefly, 4T1 tumor-bearing mice were injected with normal saline, Tf-Te, and Tf-Te/HCQ through the tail vein. The dosage of Te was 1 mg/kg. 8 h after administration, the tumor site was irradiated with NIR laser (2 W/cm^2) for 1 min. The temperature change of tumor tissue was measured and recorded by an infrared thermal imager.

2.20. *In vivo biosafety evaluation*

During the antitumor treatment period, the body weight of tumor-bearing mice was recorded. At the end of treatment, the mice were sacrificed, and the weight of major organs was measured to evaluate the organ index. Moreover, the blood samples were collected for blood routine analysis and biochemical tests, to evaluate the hematological toxicity, liver function, and kidney function. In addition, the hemolytic effect of Tf-Te/HCQ was studied to evaluate its hematotoxicity. In brief, Tf-Te/HCQ suspensions with different concentrations (3, 6, 12, and 24 μg/mL) were mixed with red blood cells, respectively. After incubation at 37 °C for 4 h and then centrifugation at 3000 rpm for 5 min, the absorbance of the supernatant was measured at 540 nmol/L. Red blood cells incubated with deionized water and PBS were set as the positive and negative control groups, respectively. The hemolysis rate was calculated using the following Eq. (6):

$$\text{Hemolysis rate}\,(\%) = (A_s - A_{nc}) / (A_{pc} - A_{nc}) \times 100 \quad (6)$$

where A_s, A_{nc} and A_{pc} represented absorbances of samples, negative control and positive control, respectively.

All experimental procedures were executed according to the protocols approved by Zhengzhou University's Animal Care and Use Committee.

2.21. Statistical analysis

All data were analyzed by GraphPad Prism6 software (GraphPad Software, San Diego, CA, USA). One-way ANOVA was used for both a multi-group comparison and a two-group comparison in multiple groups. $^{*}P < 0.05$, $^{**}P < 0.01$, and $^{***}P < 0.001$ were considered as statistically significant.

3. Results and discussion

3.1. Synthesis and characterization of Tf-Te/HCQ

Tf-Te NPs were synthesized using Tf as the PROTEIN mineralization template. TEM and DLS analysis (Fig. 1A and B) showed that Tf-Te NPs had a uniform particle size of 32.6 nmol/L (PDI: 0.274). After hydrophobic HCQ loading, the particle size of Tf-Te/HCQ increased. The TEM image in Fig. 1C proves that the structure of Tf-Te/HCQ was relatively loose and composed of multiple small NPs. DLS analysis further showed that the hydrated particle size of Tf-Te/HCQ was 213 nmol/L with a PDI of 0.352 (Fig. 1D and Supporting Information Fig. S1). In addition, after HCQ loading, the zeta potential of NPs changed from −12.8 (Tf-Te) to −21.3 mV (Tf-Te/HCQ) (Supporting Information Fig. S2). All the above results demonstrated that the loading of hydrophobic HCQ can change the morphology, particle size, and zeta potential of biomimetic mineralized Te NPs. Moreover, the UV−vis spectrum (Fig. 1E) showed that Tf-Te NPs had a specific absorption peak at 278 nmol/L and a wide absorption range from 400 to 850 nmol/L, which were assigned to the characteristic absorption of Tf and Te, respectively. After HCQ loading, an absorption peak at 330 nmol/L appeared on the spectrum of Tf-Te/HCQ, which was assigned to the characteristic absorption of HCQ. These characteristic absorption peaks all proved the successful synthesis of Tf-Te/HCQ. More importantly, the NIR absorption capacity of Te at 808 nmol/L was not affected after HCQ loading. In addition, the total sulfhydryl assay kit was used to monitor the reaction process. As Fig. 1F shown, the concentration of sulfhydryl groups in the solution increased from 13.74 to 478.5 μg/mL after the addition of reduced GSH, suggesting that reduced GSH can efficiently open the intramolecular disulfide bond of Tf. After mineralization with Na_2TeO_3, sulfhydryl groups decreased to 6.92 μg/mL, because oxidizing Na_2TeO_3 can react with reductive sulfhydryl groups on Tf to form the intermolecular disulfide bond between different Tf molecular. This result further proved that Tf-Te/HCQ can be successfully synthesized by disulfide bond reconstruction technology. Moreover, XPS analysis was adopted to explore the valence states of Te in Tf-Te/HCQ. As shown in Fig. 1G, the characteristic peaks of Te $3d_{3/2}$ and Te $3d_{5/2}$ at 584.58 and 574.16 eV with good spin−orbit components (Δmetal = 10.4 eV) proved that Te was zero-valent. Furthermore, the XRD spectrum showed that Te in Tf-Te/HCQ presented characteristic Bragg peaks at (011) and (102) planes (Fig. 1H), suggesting that Te had a crystalline structure. Compared with amorphous disorder and resistance drift, Te with

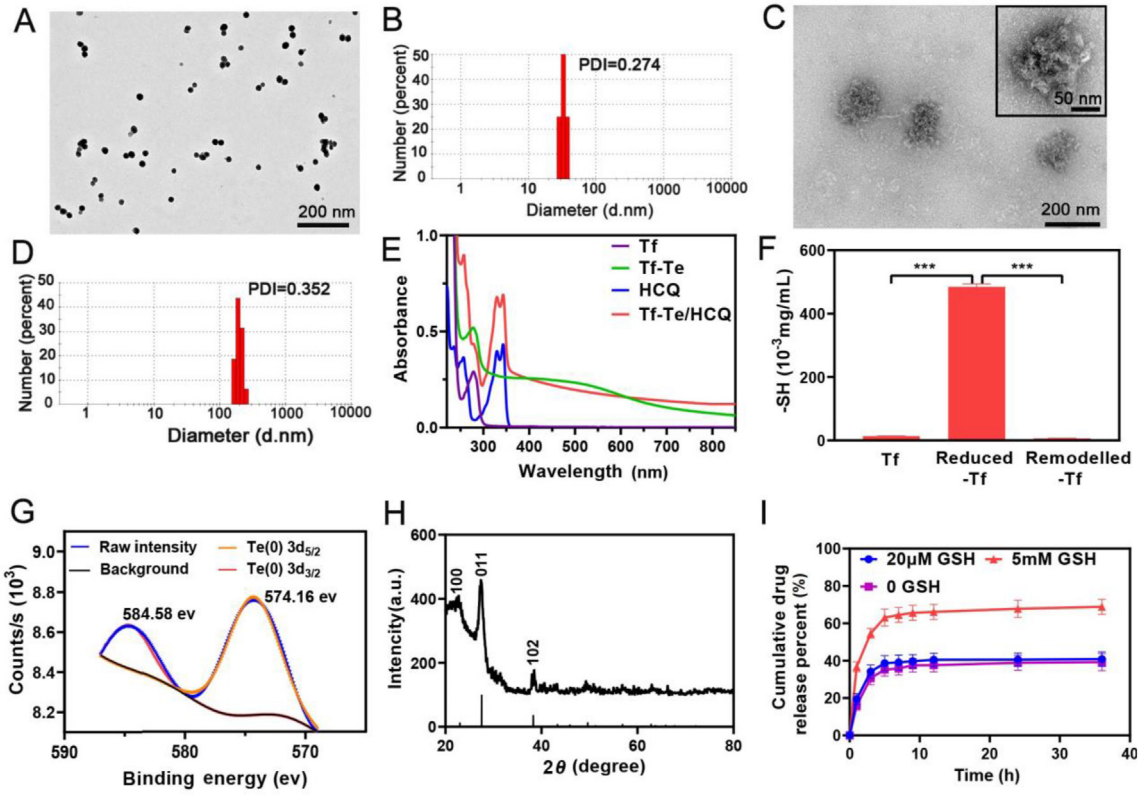

Figure 1 Characterization of Tf-Te/HCQ. (A) TEM image of Tf-Te NPs. (B) Particle size distribution of Tf-Te NPs. (C) TEM images of Tf-Te/HCQ. (D) Particle size distribution of Tf-Te/HCQ. (E) UV−Vis wavelength scanning spectra of Tf, HCQ, Tf-Te NPs and Tf-Te/HCQ. (F) Changes of total sulfhydryl groups in solution before and after Tf-Te/HCQ synthesis ($n = 3$, $^{***}P < 0.001$). (G) XPS spectra of Tf-Te/HCQ. (H) XRD pattern of Tf-Te/HCQ. (I) Cumulative drug release percentage of Tf-Te/HCQ NPs in different environments ($n = 3$).

crystalline structure has better photothermal stability. Furthermore, Tf-Te/HCQ exhibited relatively good dispersibility in PBS, serum, and RPMI 1640 medium (Supporting Information Fig. S3), guaranteeing stability during drug delivery *in vivo*. Meanwhile, there was no obvious particle size and zeta potential change in the PBS solution for 7 days (Supporting Information Fig. S4), indicating its excellent pharmaceutical stability in a physiological medium.

Next, drug loading capacity and GSH responsive drug release profile of Tf-Te/HCQ were investigated. Firstly, the feeding ratio of Tf: HCQ was optimized to get high drug loading and encapsulation efficiency. As seen in Supporting Information Fig. S5, when the feeding ratio of Tf: HCQ was 4:1, the loading and encapsulation efficiency of HCQ were 5.4% and 28.1%, respectively, indicating that Tf with hydrophobic cavity structure can be used as an excellent cargo for HCQ loading. Subsequently, the GSH-responsive drug release profile of Tf-Te/HCQ was investigated. As we know, the concentrations of GSH in blood (0 μmol/L), tumor microenvironment (2−20 μmol/L), and tumor cells (5−10 mmol/L) are very different. Therefore, we prepared different drug release mediums with GSH concentrations of 0, 20 μmol/L, and 5 mmol/L to simulate blood, tumor microenvironment, and tumor cells, respectively. As seen in Fig. 1I, the cumulative drug release percentages of HCQ at 36 h were 39.2%, 41.6%, and 68.2% when the concentrations of GSH were 0, 20 μmol/L and 5 mmol/L, respectively. This result indicated that Tf-Te/HCQ had an obvious GSH-responsive drug release profile, which was attributed to the GSH-responsive disintegration feature of Tf-Te/HCQ shown in Supporting Information Fig. S6.

3.2. *The photothermal and photodynamic performance of Tf-Te/HCQ*

For tumor phototherapy, the photothermal conversion and photodynamic properties of photosensitizers are key factors affecting the therapeutic effect. Firstly, the photothermal conversion capacity of Tf-Te/HCQ was evaluated in an aqueous solution. As Fig. 2A shown, the temperature of Tf-Te and Tf-Te/HCQ suspensions can rise above 60 °C after irradiation for 5 min at 2 W/cm^2. In addition, Fig. 2B and C proved that the temperature rises of Tf-Te and Tf-Te/HCQ presented significant concentration- and irradiation time-dependent characteristics. Moreover, 30 μg/mL of Tf-Te and Tf-Te/HCQ suspensions were exposed to 808 nmol/L laser with different output power (1, 1.5, 2, 2.5 W/cm^2) for 5 min. As shown in Fig. 2D and E, the temperature of Tf-Te/HCQ rose to 55.0 and 92.6 °C after irradiation under 808 nmol/L laser for 5 min at 1 and 2.5 W/cm^2, respectively, exhibiting a significant power-dependent model. Overall, the

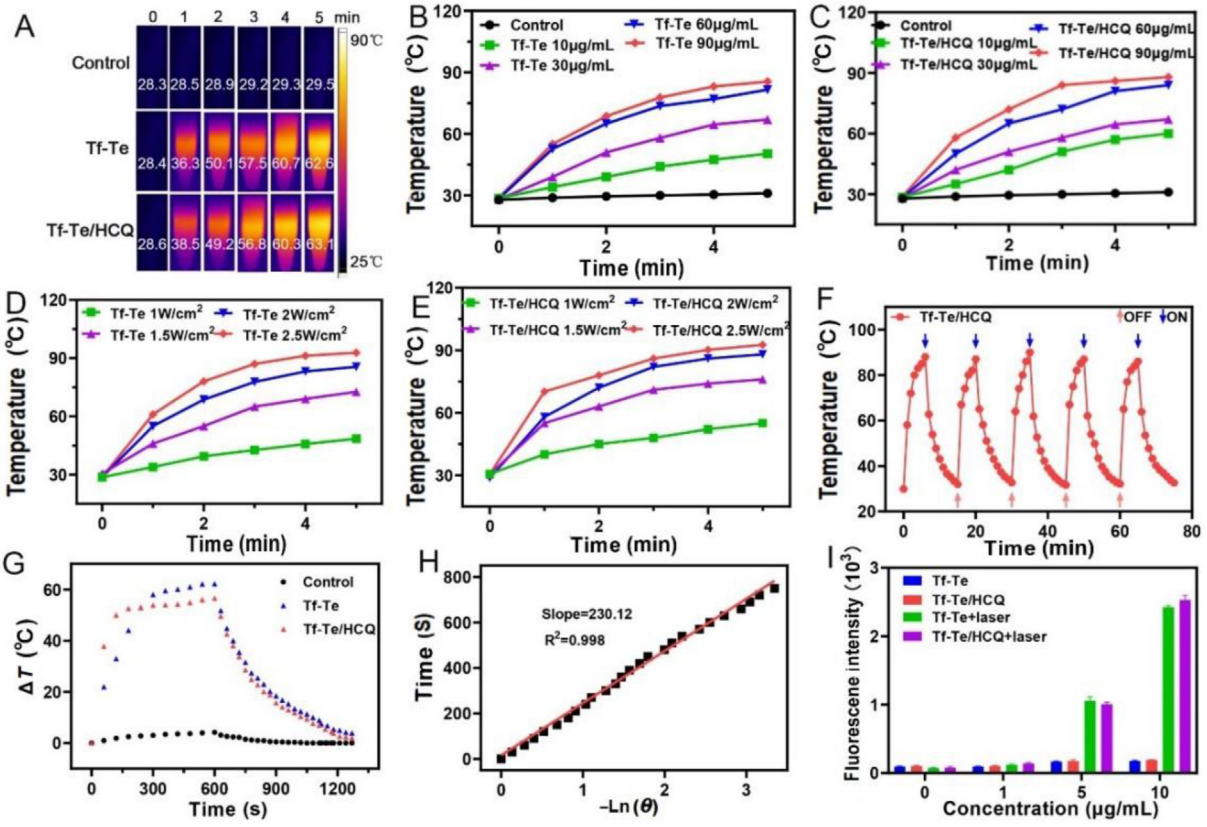

Figure 2 The photothermal and photodynamic performance of Tf-Te/HCQ. (A) The near infrared thermal imaging photos of Tf-Te and Tf-Te/HCQ under 808 nm laser irradiation. (B) The temperature change curve of Tf-Te with different concentrations at different irradiation time. (C) The temperature change curve of Tf-Te/HCQ with different concentrations at different irradiation time. (D) Influence of output power on temperature rise of Tf-Te NPs. (E) Influence of output power on temperature rise of Tf-Te/HCQ. (F) Photothermal stability performance of Tf-Te/HCQ for 5 on/off cycles. (G) The temperature variation of Tf-Te and Tf-Te/HCQ in heating and cooling processes. (H) Plot of cooling time *in situ* temperature. −Lnθ obtained from the cooling time of Tf-Te/HCQ. (I) The ROS generation ability of Tf-Te and Tf-Te/HCQ with or without 808 nm laser irradiation (n = 3).

photothermal conversion effect of Tf-Te/HCQ demonstrated obvious concentration-, output power- and irradiation time-dependent pattern, which was beneficial to exert anti-tumor effect.

Next, the photostability of Tf-Te/HCQ was evaluated. In brief, Tf-Te/HCQ suspension was irradiated at 2 W/cm^2 for 5 min, then cooled to room temperature without irradiation and irradiated/cooled for 4 more cycles. Fig. 2F and Supporting Information Fig. S7 demonstrate that the photothermal effect of Tf-Te/HCQ was well preserved under 5 cycles of on/off NIR laser irradiation. Fig. 2G showed the temperature variation of Tf-Te/HCQ in the above heating and cooling process. During the heating process, the temperature of Tf-Te/HCQ suspension can rapidly rise to over 42 °C, which can meet the requirements of tumor hyperthermia. Based on the data in Fig. 2G and H, the photothermal conversion efficiency (η) of Tf-Te/HCQ was calculated as 63.22%. In addition, the DCFH-DA ROS probe was used to evaluate the ROS generation efficiency of Tf-Te/HCQ under NIR irradiation. As Fig. 2I shown, in the absence of laser irradiation, there were very weak fluorescence signals in Tf-Te and Tf-Te/HCQ groups, suggesting no ROS generation. However, after 3 min of laser irradiation, the fluorescence signal of Tf-Te and Tf-Te/HCQ (Te = 10 μg/mL) was 14.1 and 13.4 times higher than that of the control group, respectively. Furthermore, ESR was utilized to determine the specific type of ROS generated by Tf-Te/HCQ NPs. As Supporting Information Fig. S8 shown, the characteristic triple, quadruple, and six-fold peaks of TEMP-$^1O_2$, DMPO-•OH, and BMPO-•O_2 were all observed, suggesting typical three types of ROS ($^1O_2$, •O_2 and •OH) can be generated by Tf-Te/HCQ under 808 nmol/L laser irradiation. All the above results indicated that Tf-Te/HCQ had good photothermal conversion and photodynamic properties, and can be used for tumor phototherapy.

3.3. *Anti-tumor effect of Tf-Te/HCQ in vitro*

High intracellular drug concentration is the key factor affecting the anti-tumor effect, so the targeting efficiency of Tf-Te/HCQ was investigated at first. As shown in Fig. 3A after incubation with FITC-labeled Tf-Te/HCQ for 6 h, there was 72.5% of Tf-Te/HCQ entering 4T1 cells, which was significantly higher than that of the free FITC group (2.16%). This was due to that Tf can specifically recognize TfR highly expressed on the surface of 4T1 cells, and thereafter Tf-Te/HCQ can enter tumor cells through TfR-mediated endocytosis.

Next, we evaluated the cytotoxicity of different formulations by CCK-8 assay. As shown in Fig. 3B and C, there was no significant difference in the cell inhibition rate in the HCQ group with and without laser irradiation. When the concentration of HCQ was 10 μg/mL, the cell inhibition rates of HCQ and HCQ + L groups were 24.1% and 25.3%, respectively. This indicated that the laser itself had no significant effect on cell activity. However, when the concentration of Te was 10 μg/mL, cell inhibition rates of Tf-Te/HCQ and Tf-Te/HCQ + L were 38.3% and 81.7%, respectively, indicating that Tf-Te/HCQ could effectively enhance the killing effect on 4T1 tumor cells under NIR laser. Furthermore, the IC50 values of HCQ + L, Tf-Te + L, and Tf-Te/HCQ + L were calculated as 334.4, 7.852, and 1.543 μg/mL, respectively (Supporting Information Fig. S9), indicating that phototherapy combining with autophagy inhibition could achieve the synergetic anti-tumor effect. Moreover, Calcein-AM/PI double staining method was used to visually observe the living and dead tumor cells after drug treatment. Supporting Information Fig. S10 shows that Tf-Te/HCQ + L group exhibited the weakest green fluorescence (living cells) and the strongest red fluorescence (dead cells), which also proved that Tf-Te/HCQ combined with NIR laser can effectively kill 4T1 tumor cells. In addition, cell survival rates of HC11 cells were all above 90% (Supporting Information Fig. S11), suggesting no obvious toxicity of Tf-Te/HCQ to normal cells. This may be due to that HC11 cells lacking TfR are unable to effectively uptake Tf-Te/HCQ nanoparticles.

3.4. *Intracellular ROS production and photothermal conversion of Tf-Te/HCQ*

To verify the PDT and PTT combined anti-tumor mechanism of Tf-Te/HCQ, intracellular ROS production and photothermal conversion abilities of Tf-Te/HCQ were further studied. As shown in Fig. 3D, there was a low ROS level in 4T1 cells treated with Tf-Te and Tf-Te/HCQ. However, intracellular fluorescence intensity significantly increased after 808 nmol/L laser irradiation. The results of semi-quantitative analysis show that the fluorescence signals of Tf-Te + L and Tf-Te/HCQ + L increased to 4.2 and 4.1 times, respectively, compared with the Control + L group (Fig. 3E). Above results indicate that Tf-Te/HCQ can produce a large amount of ROS in 4T1 cells under laser irradiation, and the addition of HCQ did not influence the ability of Te to produce ROS. Next, we evaluated the intracellular photothermal conversion ability of Tf-Te/HCQ by monitoring the temperature change of 4T1 tumor cells pre-treated with Tf-Te or Tf-Te/HCQ before and after 808 nmol/L laser stimulation. As Fig. 3F shown, after laser irradiation, the cell temperature of the Control + L group increased to 35.8 °C, while Tf-Te + L and Tf-Te/HCQ + L groups increased to 45.7 and 48.9 °C, respectively. The temperature difference analysis (Fig. 3G) showed that the temperature of the Control + L group increased by 1.1 °C after laser irradiation for 3 min, while that of the Tf-Te + L and Tf-Te/HCQ + L groups increased by 10.6 and 11.4 °C, respectively, which can meet the requirements of tumor hyperthermia. All the above results proved that Tf-Te/HCQ can synchronously generate a large amount of ROS and sufficient heat within tumor cells under 808 nmol/L laser irradiation, thereby achieving the combined PTT and PDT anti-tumor effect.

3.5. *Autophagy inhibition effect induced by Tf-Te/HCQ according to lysosomal damage pathway*

Firstly, the lysosomotropic activity of Tf-Te/HCQ was studied according to monitor intracellular localization of Tf-Te/HCQ. Briefly, after 4T1 cells were incubated with FITC-labeled Tf-Te/HCQ for different times, lysosomes were stained with Lyso-Tracker Red to observe the colocalization performance of Tf-Te/HCQ with lysosomes. As shown in Supporting Information Fig. S12, after entering 4T1 cells, Tf-Te/HCQ@FITC can be precisely positioned in lysosomes. The colocalization coefficients of Tf-Te/HCQ with lysosomes at 4 and 6 h were 0.52 ± 0.06 and 0.71 ± 0.07, respectively, indicating that Tf-Te/HCQ had good lysosomal colocalization performance. Next, we evaluated the lysosome damage effect of Tf-Te/HCQ under 808 nmol/L laser irradiation. As shown in Fig. 4A and Supporting Information Fig. S13, after 6 h of administration, HCQ and Fe^{2+} alone can both induce lysosome damage effect, and the Lyso-Tracker-stained red flecks in Tf-Te/HCQ treated cells were significantly less than those in HCQ, Fe^{2+}, and Tf-Te treated cells. Moreover, the fluorescence

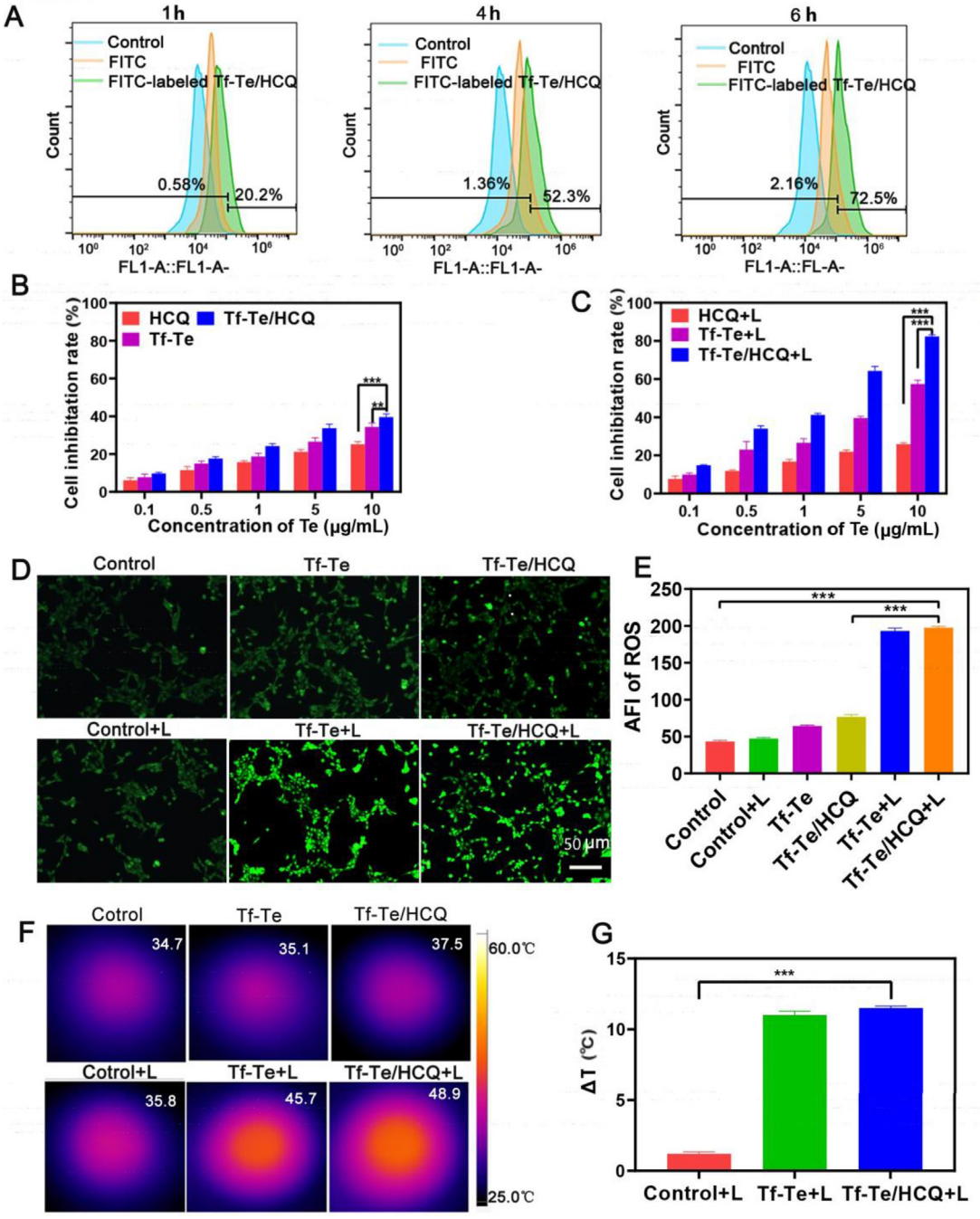

Figure 3 Anti-tumor effect of Tf-Te/HCQ *in vitro*. (A) The intracellular uptake results after 4T1 cells incubation with FITC and FITC-labeled Tf-Te/HCQ nanoparticles for 1, 4, and 6 h. (B) The tumor inhibition rate of different preparations without 808 nm laser irradiation for 24 h ($n = 6$, $^{**}P < 0.01$, $^{***}P < 0.001$). (C) The tumor inhibition rate of different preparations with 808 nm laser irradiation for 24 h ($n = 6$, $^{***}P < 0.001$). (D) Intracellular ROS production of different treatment groups (Te = 10 μg/mL). (E) The semi-quantitative fluorescence intensity of intracellular ROS ($n = 3$, $^{***}P < 0.001$). (F) The temperature of Tf-Te and Tf-Te/HCQ (Te = 10 μg/mL) treated cells before and after 808 nm laser irradiation. (G) The temperature difference in Control + L, Tf-Te + L and Tf-Te/HCQ + L groups ($n = 3$, $^{***}P < 0.001$).

semiquantitative analysis result (Fig. 4B) further revealed that the red fluorescence signal in the Control + L group was strong, with an average fluorescence intensity of 118.2. The average fluorescence intensity in HCQ + L and Tf-Te + L groups was 58.4 and 87.5, respectively. Particularly, 4T1 cells treated with Tf-Te/HCQ demonstrated the weakest red fluorescence with a fluorescence intensity of 33.56, indicating that Tf-Te/HCQ had the strongest lysosomal damage effect. This high lysosomotropic activity of Tf-Te/HCQ may be attributed to the following three reasons. Firstly, Tf-Te/HCQ can efficiently enter 4T1 tumor cells through TfR-mediated endocytosis to increase intracellular HCQ accumulation. Secondly, Tf-Te/HCQ had specific localization and retention performance in lysosomes after entering tumor cells. As we know, the lysosome is the target effector organelle

of HCQ. Therefore, Tf-Te/HCQ could transfer HCQ to its targeted organelle directly. Thirdly, the disulfide bonds crosslinked inside Tf-Te/HCQ broke down in response to high GSH levels in 4T1 tumor cells, and Tf-Te/HCQ disintegrated to simultaneously release Fe^{2+} and HCQ at fixed points (Supporting Information Fig. S14). They then triggered lysosomal alkalinization (Supporting Information Fig. S15) and elevated osmotic pressure, synergistically leading to lysosomal destruction.

Normal lysosomal structure and function are required for autophagy to proceed. The destruction of lysosomes can further lead to effective autophagy inhibition during the digestive stage of autophagic flux. Therefore, next, we investigated the autophagy inhibition effect of Tf-Te/HCQ on 4T1 tumor cells by Western blotting method and immunofluorescence analysis. As we know, when autophagy is inhibited, LC3-I is converted into LC3II, and a large amount of LC3II accumulates, resulting in an increased LC3II/LC3-I ratio. Meanwhile, autophagy inhibition is usually accompanied by the accumulation of autophagy substrate p62 PROTEIN. As shown in Fig. 4C and D, the ratio of LC3-II/LC3-I and p62 levels in the Tf-Te/HCQ group were significantly increased compared with the Control group. The numerical values of LC3-II/LC3-I and p62 in the Tf-Te/HCQ + L group were 1.4 and 1.5 times higher than those in Control + L group, respectively. This was because HCQ can inhibit the fusion and degradation of autophagosomes and lysosomes, thereby inhibiting autophagy. In addition, the ratio of LC3-II/LC3-I in the Tf-Te + L group was 1.2 times higher than that in the Control + L group, while the expression level of p62 in the Tf-Te + L group was 0.67 times that of the Control + L group, indicating that autophagy was activated in Tf-Te + L group without HCQ treatment. The above results indicated that HCQ can exert an inhibitory effect on autophagy induced by Tf-Te mediated PTT/PDT, thus achieving the synergistic anti-tumor effect of autophagy inhibition and phototherapy. Moreover, the immunofluorescence analysis was carried out to further verify this conclusion. As shown in Fig. 4E and F, the fluorescence of LC3 and p62 in Tf-Te/HCQ + L group was 3.2 and 2.5 times higher than that in Control + L group, while the fluorescence of LC3 and p62 in Tf-Te + L group was 2.3 and 0.4 times higher than that in Control + L group. This was consistent with the Western blot results, further proving the autophagosome accumulation effect caused by Tf-Te/HCQ.

3.6. *Tumor targeting ability and metabolism behavior of Tf-Te/HCQ in vivo*

Tf-Te/HCQ was labeled with NIR fluorescent dye IR780 for real-time tracking of its distribution in the body. As shown in Fig. 5A, free IR780 lacked tumor targeting ability and its fluorescence intensity decreased rapidly over time. While Tf-Te/HCQ@IR780 tended to accumulate at the tumor site. At 24 h after injection, major organs and tumor tissues were dissected for *ex vivo* imaging. As Fig. 5B shown, Tf-Te/HCQ@IR780 was mainly distributed in tumor tissues. semi-quantitative analysis showed that the fluorescence intensity of tumor tissue in the Tf-Te/HCQ@IR780 group was 2.04 times higher than that in the free IR780 group (Fig. 5C), further indicating the excellent *in vivo* tumor targeting ability of Tf-Te/HCQ. In addition, as Supporting Information Fig. S16 shown, except for tumor tissue, the liver and lung are the other two major tissues with a high distribution of Tf-Te/HCQ. To explore the reason for the above phenomenon, the visual cellular uptake behavior of Tf-Te/HCQ by RAW264.7 macrophages and 4T1 cells was studied using CLSM. As Supporting Information Figs. S17 and S18 shown, Tf-Te/HCQ can be uptake by both macrophages and 4T1 cells, and cellular uptake efficacy of 4T1 tumor cells was significantly higher than that of macrophages. Therefore, after intravenous administration, Tf-Te/HCQ mainly accumulated in tumor tissues, followed by liver and lung tissues. Moreover, Supporting Information Fig. S19 exhibited that the plasma concentration of Te gradually decreased along with time, and it became fairly low at 48 h after administration. This suggested that Tf-Te/HCQ can't accumulate in large quantities *in vivo* and cause toxicity.

3.7. *In vivo anti-tumor effect*

Next, we investigated the anti-tumor efficiency of Tf-Te/HCQ in 4T1 tumor-bearing mice. As revealed in Fig. 5D, the relative tumor volume of the control group increased significantly during the treatment period. HCQ + L, Tf-Te, Tf-Te + L, and Tf-Te/HCQ groups all showed a certain tumor inhibitory effect. Moreover, the Tf-Te/HCQ + L group demonstrated the best anti-tumor effect, with the lowest tumor weight (Fig. 5E) and smallest tumor size (Supporting Information Fig. S20). In addition, H&E staining results of tumor tissues further showed that the tumor cells in Tf-Te/HCQ + L group were necrotic significantly, compared with those in other groups, indicating that Tf-Te/HCQ + L had an outstanding anti-tumor effect *in vivo* (Fig. 5F).

3.8. *The autophagy inhibition effect in vivo*

At the end of the pharmacodynamic experiment, tumor tissues of mice in each group were collected for immunofluorescence analysis, to measure the expression of autophagy-associated PROTEIN LC3 and p62 (Fig. 6A and B). Fluorescence semi-quantitative analysis (Fig. 6C) showed that the LC3-II/LC3-I ratio and p62 level of the Tf-Te + L group were 1.2 and 0.67 times higher than that of the Control + L group, respectively (Fig. 6D), indicating that Tf-Te + L mediated phototherapy can activate tumor autophagy. However, the LC3-II/LC3-I ratio and p62 level in the Tf-Te/HCQ + L group were 1.4 and 1.5 times higher than that in the Control + L group, respectively, revealing that tumor autophagy was obviously inhibited. The above results indicated that Tf-Te/HCQ can effectively inhibit tumor autophagy induced by Tf-Te-mediated PTT/PDT treatment.

3.9. *ROS generation and photothermal conversion ability of Tf-Te/HCQ in vivo*

Firstly, we studied the ROS generation ability of Tf-Te/HCQ in 4T1 tumor tissues. The results demonstrated that ROS level in Tf-Te + L and Tf-Te/HCQ + L treated tumor tissues was much higher than that in the other groups (Fig. 6E). The fluorescence intensity of Tf-Te/HCQ + L group was 3.6 times that of the Control + L group (Fig. 6F), indicating that Tf-Te/HCQ could produce a large amount of ROS in the tumor tissue under 808 nmol/L laser irradiation. Furthermore, we investigated the photothermal conversion ability of Tf-Te/HCQ *in vivo*. As Fig. 6G and H shown, after NIR laser irradiation, the temperature of tumor tissue in the Control group increased from 36.8 to 38.6 °C, and there was no significant change observed.

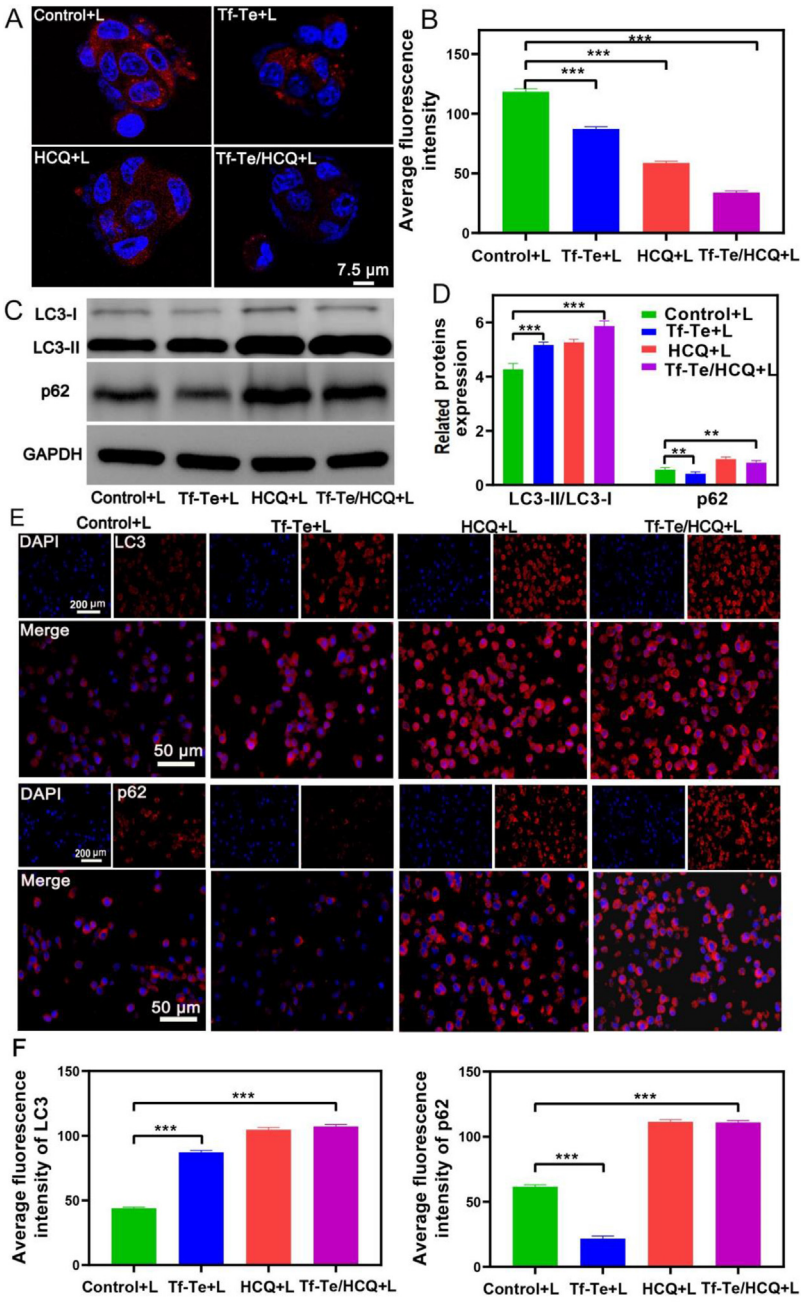

Figure 4 The autophagy inhibition effect of Tf-Te/HCQ in 4T1 cells. (A) Confocal imaging results of 4T1 cells treated with different preparations for 6 h (Blue: DAPI stained nuclear, Red: Lyso-Tracker Red stained lysosome flecks). (B) Red lysosome fluorescence intensity in 4T1 cells treated with different preparations for 6 h ($n = 3$, $^{**}P < 0.01$, $^{***}P < 0.001$). (C) Western blot analysis of autophagy-related PROTEINS (LC3-I, LC3-II, p62) in 4T1 cells after treatment with Tf-Te + L, HCQ + L and Tf-Te/HCQ + L. (D) The semi-quantitative analysis of LC3-II/LC3-I and p62 PROTEIN bands ($n = 3$, $^{***}P < 0.001$). (E) Immunofluorescence images of LC3 and p62 in 4T1 cells treated with different preparations for 6 h. (F) Semi-quantitative analysis of LC3 and p62 in 4T1 cells ($n = 3$, $^{***}P < 0.001$).

However, the temperature of tumor tissue treated with Tf-Te and Tf-Te/HCQ rapidly increased to 49.8 and 50.6 °C, respectively, indicating that Tf-Te/HCQ had excellent photothermal conversion characteristics *in vivo*. All these results proved that Tf-Te/HCQ can be used for tumor PTT/PDT synergistic treatment *in vivo*.

3.10. In vivo biosafety evaluation

Finally, the *in vivo* biosafety of Tf-Te/HCQ was studied. As seen in Fig. 7A, there was no significant difference in body weight among all groups during administration, indicating that Tf-Te/HCQ had no obvious system toxicity. In addition, there was no

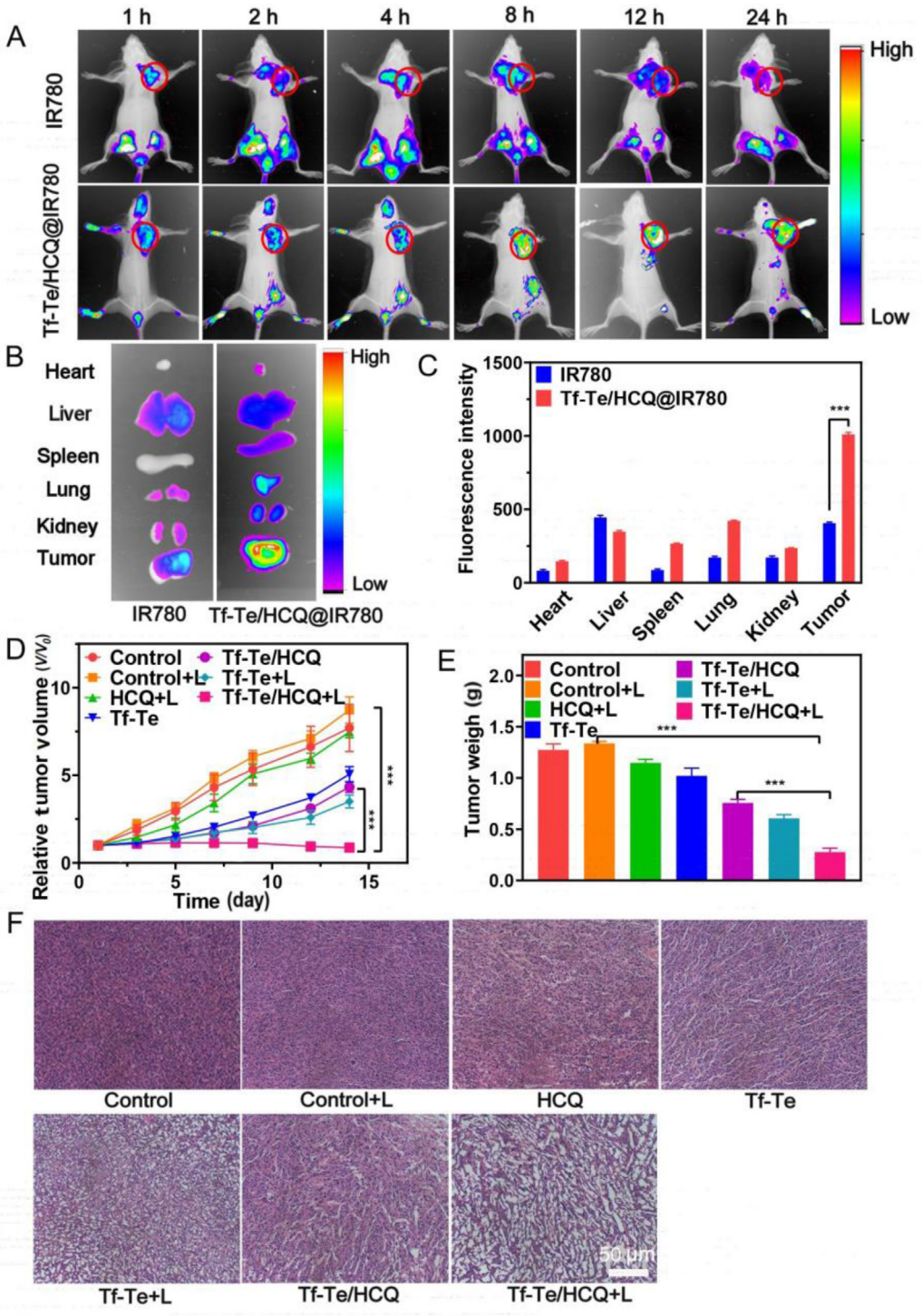

Figure 5 Anti-tumor effect of Tf-Te/HCQ in 4T1 tumor-bearing mice. (A) *In vivo* NIR imaging of 4T1 tumor-bearing mice after intravenous injection of free IR780 and IR780-labeled Tf-Te/HCQ at 1, 2, 4, 8, 12 and 24 h post injection. (B) *Ex vivo* NIR imaging of various major tissues in different groups at 24 h post injection. (C) Fluorescence semi-quantitative analysis of isolated organs at 24 h post injection ($n = 6$, $^{***}P < 0.001$). (D) Tumor volume changes of mice treated with different formulations within two weeks ($n = 6$, $^{***}P < 0.001$). (E) Tumor weights for each treatment group at the end of the pharmacodynamic experiment ($n = 6$, $^{***}P < 0.001$). (F) H&E staining result of tumor tissues that harvested from mice after two weeks of treatment with different formulations.

significant difference in the viscera coefficient of mice, as shown in Fig. 7B. Blood biochemical indicators, such as AST, ALT, and UREA, were used to evaluate the liver and kidney functions of mice (Fig. 7C and D). Meanwhile, blood routine indicators, such as WBC, RBC, and PLT were used to further evaluate the blood toxicity (Fig. 7E and F). As Fig. 7C−F shown, there was no significant difference in these indexes between Tf-Te/HCQ + L and Control groups, indicating that Tf-Te/HCQ + L had good

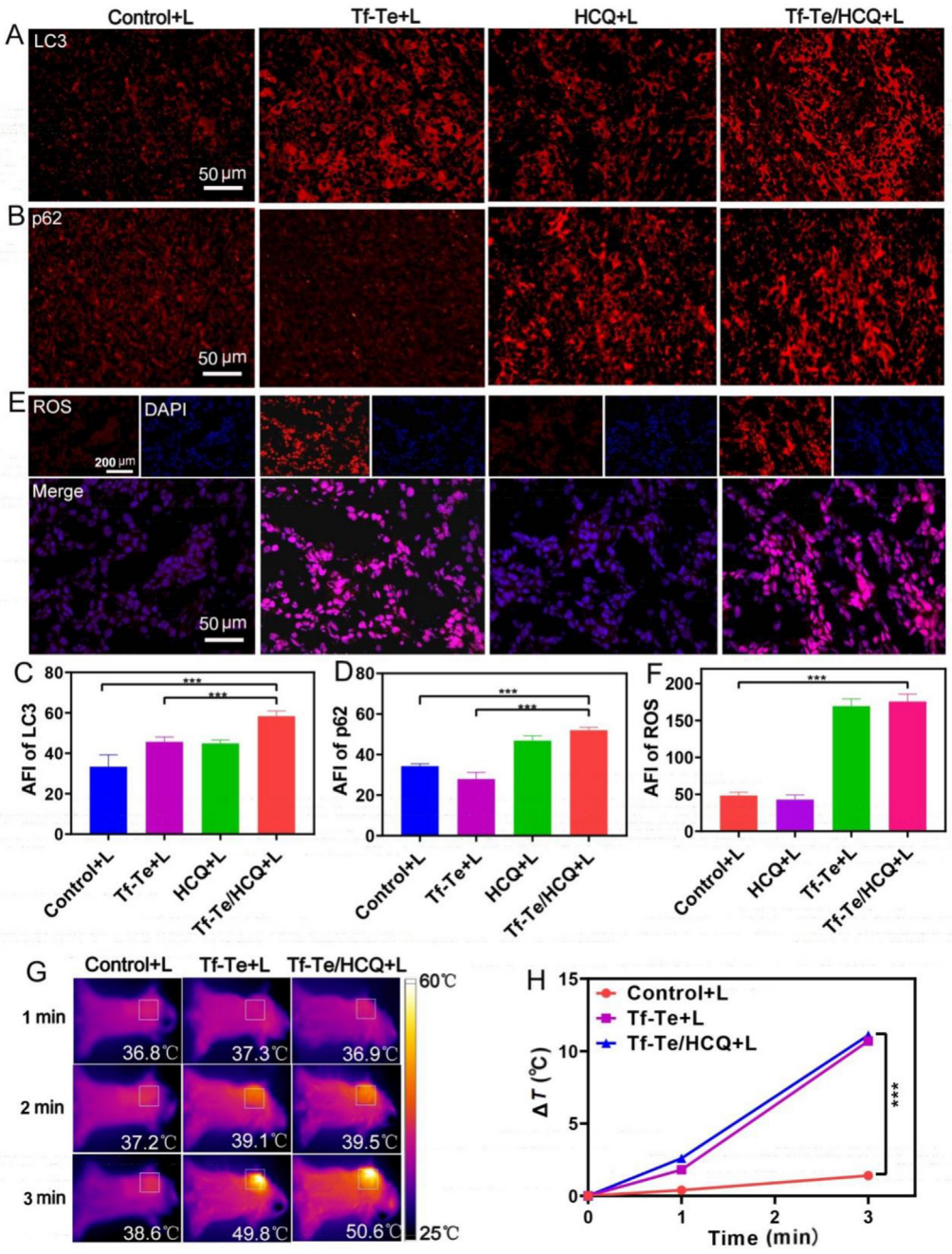

Figure 6 Anti-tumor mechanism of Tf-Te/HCQ in 4T1 tumor-bearing mice. (A) Immunofluorescence results of LC3 PROTEIN in tumor tissues after treatment with different formulations. (B) Immunofluorescence results of p62 PROTEIN in tumor tissues after treatment with different formulations. (C) Mean fluorescence intensity of LC3 PROTEIN in tumor tissues after treatment with different formulations ($n = 6$, $^{***}P < 0.001$). (D) Mean fluorescence intensity of p62 PROTEIN in tumor tissues after treatment with different formulations ($n = 6$, $^{***}P < 0.001$). (E) ROS production in tumor tissues after treatment with different formulations for 8 h. (F) Mean fluorescence intensity of ROS in tumor tissues after treatment with different formulations for 8 h ($n = 6$, $^{***}P < 0.001$). (G) The temperature of tumor tissues in different groups after 808 nm laser irradiation for 1 and 3 min. (H) Temperature difference map of tumor tissues in each group ($n = 6$, $^{***}P < 0.001$).

biocompatibility *in vivo*. Furthermore, toxicity in major organs was also evaluated by H&E staining (Fig. 7G). No obvious pathological changes were observed in the heart, liver, spleen, lung, and kidney tissues of mice after treatment with Tf-Te/HCQ, further proving the excellent biosafety of Tf-Te/HCQ. Supporting Information Fig. S21 exhibited that the hemolysis rates of Tf-Te/HCQ with various concentrations were much lower than the upper limited value of 5%, confirming its excellent blood compatibility. All the above results suggested that Tf-Te/HCQ can be used as a safe nanomedicine for tumor treatment *in vivo*.

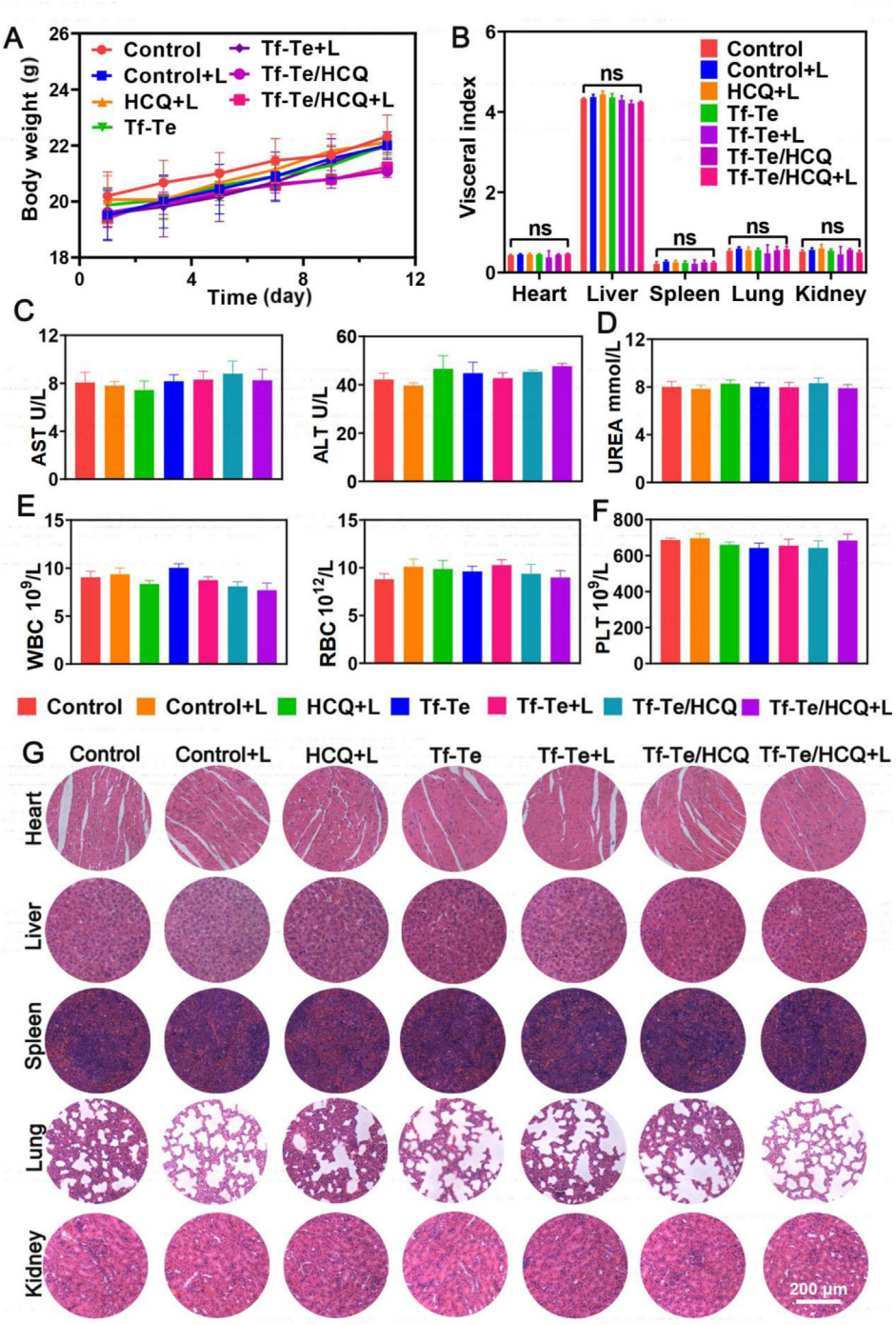

Figure 7 *In vivo* safety evaluation of Tf-Te/HCQ. (A) Body weight changes of mice in each group during two weeks treatment ($n = 6$). (B) The viscera coefficient of mice in each group after treatment ($n = 6$). (C−F) Blood biochemical parameters and blood routine examination after different treatments ($n = 6$). (G) H&E staining results of major organs in different treatment groups.

4. Conclusions

In summary, this work suggested a novel strategy for breast tumor treatment by integrating PTT/PDT synergistic therapy with autophagy inhibition. An intelligent nano platform Tf-Te/HCQ was constructed which can specifically target tumors and achieve GSH-responsive drug release. *In vivo* and *in vitro* experiments showed that Tf-Te/HCQ can produce a large amount of heat and ROS under NIR laser irradiation. Meanwhile, simultaneously released HCQ and Fe^{2+} in tumor cells efficiently inhibited autophagy by increasing the osmotic pressure and pH in lysosomes, thereby synergistically enhancing the therapeutic effect of tumor phototherapy.

Acknowledgments

This work was supported by the National Natural Science Foundation of China (Nos. 82102918, 81972893 and 82172719), the

Key Program for Science and Technology Research in Henan Province (No. 232102311093, China) and the Training Plan for Young Backbone Teachers in Higher Education Institutions of Henan Province (No. 2021ZDGGJS054, China).

Author contributions

Huijuan Zhang, Junbiao Chang, Zhenzhong Zhang, and Lin Hou designed the research. Huijuan Zhang and Xiangyang Xuan carried out the experiments and performed data analysis. Yaping Wang, Zijun Qi, Kexuan Cao, Yingmei Tian, and Chaoqun Wang participated in part of the experiments. Junbiao Chang and Zhenzhong Zhang provided experimental drugs and quality control. Xiangyang Xuan and Huijuan Zhang wrote the manuscript. Lin Hou and Zhenzhong Zhang revised the manuscript. All of the authors have read and approved the final manuscript.

Conflicts of interest

The authors have no conflicts of interest to declare.

Appendix A. Supporting information

Supporting data to this article can be found online at https://doi.org/10.1016/j.apsb.2023.11.019.

References

1. Zhou Y, Tong F, Gu WL, He SQ, Yang XT, Li JM, et al. Co-delivery of photosensitizer and diclofenac through sequentially responsive bilirubin nanocarriers for combating hypoxic tumors. *Acta Pharm Sin B* 2022;**12**:1416−31.
2. Ma SH, Xie J, Wang L, Zhou ZL, Luo X, Yan JH, et al. Hetero-core-shell BiNS-Fe@Fe as a potential theranostic nanoplatform for multimodal imaging-guided simultaneous photothermal-photodynamic and chemodynamic treatment. *ACS Appl Mater Int* 2021;**13**:10728−40.
3. Cai Q, Wang C, Gai SL, Yang PP. Integration of Au nanosheets and GdOF: Yb, Er for NIR-I and NIR-II light-activated synergistic theranostics. *ACS Appl Mater Int* 2022;**14**:3809−24.
4. Tian SC, He JL, Liu D, Li S, Xu QH. Aggregation enhanced photoactivity of photosensitizer conjugated metal nanoparticles for multimodal imaging and synergistic phototherapy below skin tolerance threshold. *Nano Today* 2022;**45**:101534.
5. Yang T, Ke HT, Wang QL, Tang Y, Deng YB, Yang H, et al. Bifunctional tellurium nanodots for photo-induced synergistic cancer therapy. *ACS Nano* 2017;**11**:10012−24.
6. Guo ZM, Liu Y, Cheng X, Wang D, Guo SB, Jia ML, et al. Versatile biomimetic cantharidin-tellurium nanoparticles enhance photothermal therapy by inhibiting the heat shock response for combined tumor therapy. *Acta Biomater* 2020;**110**:208−20.
7. Dominguez-Alvarez E, Racz B, Marc MA, Nasim MJ, Szemeredi N, Viktorova J, et al. Selenium and tellurium in the development of novel small molecules and nanoparticles as cancer multidrug resistance reversal agents. *Drug Resist Updat* 2022;**63**:100844.
8. Duan LQ, Liu T, Chen TF. Near-infrared laser-triggered drug release in a tellurium nanosystem for simultaneous chemo-photothermal cancer therapy. *Biomater Sci* 2021;**9**:1767−78.
9. Yang BW, Ding L, Yao HL, Chen Y, Shi JL. A Metal-organic framework (MOF) fenton nanoagent-enabled nanocatalytic cancer therapy in synergy with autophagy inhibition. *Adv Mater* 2020;**32**:e1907152.
10. Yang BW, Ding L, Chen Y, Shi JL. Augmenting tumor-starvation therapy by cancer cell autophagy inhibition. *Adv Sci* 2020;**7**:1902847.
11. Xie R, Ruan SB, Liu JQ, Qin L, Yang CY, Tong F, et al. Furin-instructed aggregated gold nanoparticles for re-educating tumor associated macrophages and overcoming breast cancer chemoresistance. *Biomaterials* 2021;**275**:120891.
12. Ruan SB, Xie R, Qin L, Yu M,N, Xiao W, Hu C, et al. Aggregable nanoparticles-enabled chemotherapy and autophagy inhibition combined with anti-PD-L1 antibody for improved glioma treatment. *Nano Lett* 2019;**19**:8318−32.
13. Zhang SY, Xie FY, Li KC, Zhang H, Yin Y, Yu Y, et al. Gold nanoparticle-directed autophagy intervention for antitumor immunotherapy *via* inhibiting tumor-associated macrophage M2 polarization. *Acta Pharm Sin B* 2022;**12**:3124−38.
14. Barth S, Glick D, Macleod KF. Autophagy: cellular and molecular mechanisms. *J Pathol* 2010;**221**:3−12.
15. Zhang HJ, Ren YP, Cao F, Chen JJ, Chen CQ, Chang JB, et al. *In situ* autophagy disruption generator for cancer theranostics. *ACS Appl Mater Int* 2019;**11**:29641−54.
16. He JY, Fan KL, Yan XY. Ferritin drug carrier (FDC) for tumor targeting therapy. *J Control Release* 2019;**311**−**312**:288−300.
17. Xu YL, Wu H, Huang J, Qian WP, Martinson DE, Ji B, et al. Probing and enhancing ligand-mediated active targeting of tumors using Sub-5 nmol/L ultrafine iron oxide nanoparticles. *Theranostics* 2020;**10**:2479−94.
18. Zhou YL, Zhou J, Wang F, Yang HF. Polydopamine-based functional composite particles for tumor cell targeting and dual-mode cellular imaging. *Talanta* 2018;**181**:248−57.
19. Wang QX, Chen X, Li ZL, Gong YC, Xiong XY. Transferrin/folate dual-targeting pluronic F127/poly(lactic acid) polymersomes for effective anticancer drug delivery. *J Biomater Sci Polym Ed* 2022;**33**:1140−56.
20. Jiang B, Chen XH, Sun GM, Chen XR, Yin YF, Jin YL, et al. A natural drug entry channel in the ferritin nanocage. *Nano Today* 2020;**35**:100948.
21. Yang Y, Hu DR, Lu Y, Chu BY, He XL, Chen Y, et al. Tumor-targeted/reduction-triggered composite multifunctional nanoparticles for breast cancer chemo-photothermal combinational therapy. *Acta Pharm Sin B* 2022;**12**:2710−30.
22. Lin CC, Huang CY, Shi ZQ, Ou MT, Sun SJ, Yu M, et al. Biodegradable calcium sulfide-based nanomodulators for H_2S-boosted Ca^{2+}-involved synergistic cascade cancer therapy. *Acta Pharm Sin B* 2022;**12**:4472−85.
23. Guo YB, Zhang YJ, Li JF, Zhang Y, Lu YF, Jiang XT, et al. Cell microenvironment-controlled antitumor drug releasing-nanomicelles for GLUT1-targeting hepatocellular carcinoma therapy. *ACS Appl Mater Int* 2015;**7**:5444−53.
24. Ruan CH, Liu LS, Lu YF, Zhang Y, He X, Chen XL, et al. Substance P-modified human serum albumin nanoparticles loaded with paclitaxel for targeted therapy of glioma. *Acta Pharm Sin B* 2018;**8**:85−96.
25. Saleh T, Soudi T, Shojaosadati SA. Redox responsive curcumin-loaded human serum albumin nanoparticles: preparation, characterization and *in vitro* evaluation. *Int J Biol Macromol* 2018;**114**:759−66.
26. Luo ZY, Tian H, Liu LL, Chen ZK, Liang RJ, Chen Z, et al. Tumor-targeted hybrid protein oxygen carrier to simultaneously enhance hypoxia-dampened chemotherapy and photodynamic therapy at a single dose. *Theranostics* 2018;**8**:3584−96.
27. Zhao W, Li AH, Chen C, Quan FY, Sun L, Zhang AT, et al. Transferrin-decorated, MoS2-capped hollow mesoporous silica nanospheres as a self-guided chemo-photothermal nanoplatform for controlled drug release and thermotherapy. *J Mater Chem B* 2017;**5**:7403−14.
28. Luo Y, Liu XP, Liang KC, Chen Q, Liu TZ, Yin B, et al. Disulfide bond reversible strategy enables gsh responsive—transferrin nanoparticles for precise chemotherapy. *Adv Ther* 2020;**3**:2000064.